



## Automatic detection of pleural effusion in chest radiographs<sup>☆</sup>



Pragnya Maduskar<sup>\*</sup>, Rick H.M.M. Philipsen, Jaime Melendez, Ernst Scholten, Duncan Chanda, Helen Ayles, Clara I. Sánchez, Bram van Ginneken

Radboud University Medical Center, Post 767, Radiology Department, PO box 9101, 6500 HB Nijmegen, The Netherlands

### ARTICLE INFO

#### Article history:

Received 7 April 2015

Revised 10 September 2015

Accepted 16 September 2015

Available online 1 December 2015

#### Keywords:

Automated

Computer-aided detection (CAD)

Pleural fluid

Tuberculosis

Costophrenic angle

### ABSTRACT

Automated detection of Tuberculosis (TB) using chest radiographs (CXRs) is gaining popularity due to the lack of trained human readers in resource limited countries with a high TB burden. The majority of the computer-aided detection (CAD) systems for TB focus on detection of parenchymal abnormalities and ignore other important manifestations such as pleural effusion (PE). The costophrenic angle is a commonly used measure for detecting PE, but has limitations. In this work, an automatic method to detect PE in the left and right hemithoraces is proposed and evaluated on a database of 638 CXRs. We introduce a robust way to localize the costophrenic region using the chest wall contour as a landmark structure, in addition to the lung segmentation. Region descriptors are proposed based on intensity and morphology information in the region around the costophrenic recess. Random forest classifiers are trained to classify left and right hemithoraces. Performance of the PE detection system is evaluated in terms of recess localization accuracy and area under the receiver operating characteristic curve (AUC). The proposed method shows significant improvement in the AUC values as compared to systems which use lung segmentation and the costophrenic angle measurement alone.

© 2015 Elsevier B.V. All rights reserved.

### 1. Introduction

Although Tuberculosis (TB) incidence has declined by 1.5% per year over the last few years, the global disease burden remains high with 9 million TB cases and 1.5 million deaths in 2013 (World Health Organization (2014)). TB is a curable disease and the major challenge lies in early detection and notification. In high-burden low-resource countries, such as in sub-Saharan Africa, individuals reporting with TB symptoms at primary-care healthcare facilities are screened using chest radiography as the first examination due to its cost effectiveness and wide availability (Story et al. (2012); Theron et al. (2012); van't Hoog et al. (2013)). Subjects with positive findings on the chest radiograph (CXR) are usually referred to more time-consuming and expensive examinations such as sputum microscopy and molecular testing for confirmatory diagnosis.

Reading CXRs for signs of active TB requires well-trained personnel and this is a scarce resource in high TB burden countries. Moreover, humans reading large numbers of CXRs are prone to fatigue.

Computer-aided detection (CAD) systems can address these issues by either assisting the readers with diagnosis (Giger et al. (2001)) or making a decision in absence of a reader (Muyoyeta et al. (2014, 2015); Jaeger et al. (2013b)). TB primarily affects the lung parenchyma and may cause diverse manifestations such as consolidations, infiltrates and cavitation (Roy and Ellis (2010)). Hence, most of the CAD systems analyze the lung fields for the presence of any parenchyma abnormalities (Hogeweg et al. (2010); Jaeger et al. (2013a)) with only some studies specifically focused on manifestations such as cavities (Shen et al. (2010); Xu et al. (2013)) or miliary TB (Koeslag and de Jager (2001)).

Extra-pulmonary TB affecting the hilum and pleura (pleural TB) is another common form of TB. Pleural TB accounted for 4% and >10% of all the TB cases in the United States (Baumann et al. (2007)) and Spain (Porcel (2009)), respectively. In this case, pleural effusion (PE) is often visible and TB is reported as one of the most common causes of PE (Porcel et al. (2014); Sutherland et al. (2012); Liam et al. (2000); Valdés et al. (1996)). The focus of our work is therefore the detection of pleural effusion (PE) in CXRs. PE is characterized by an abnormal amount of fluid accumulated in the pleural space, as shown in Fig. 1. Due to gravity, the fluid is located in the lower portions of the pleural cavity, defined as costophrenic (CP) recess. This is the region formed by the diaphragm and the chest wall and is the potential area to be analyzed for presence of PE.

As current CAD systems for TB detection are not specifically trained to analyze the CP recess, they may fail to detect TB if PE is the

<sup>☆</sup> This paper was recommended for publication by Dr. Nicholas Ayache.

<sup>\*</sup> Corresponding author.

E-mail addresses: [pragnya.m@gmail.com](mailto:pragnya.m@gmail.com), [pragnya.maduskar@radboudumc.nl](mailto:pragnya.maduskar@radboudumc.nl) (P. Maduskar), [rick.philipsen@radboudumc.nl](mailto:rick.philipsen@radboudumc.nl) (R.H.M.M. Philipsen), [jaime.melendezrodriguez@radboudumc.nl](mailto:jaime.melendezrodriguez@radboudumc.nl) (J. Melendez), [ernst.scholten@radboudumc.nl](mailto:ernst.scholten@radboudumc.nl) (E. Scholten), [duncanchanda@gmail.com](mailto:duncanchanda@gmail.com) (D. Chanda), [Helen@zambart.org.zm](mailto:Helen@zambart.org.zm) (H. Ayles), [clara.sanchezgutierrez@radboudumc.nl](mailto:clara.sanchezgutierrez@radboudumc.nl) (C.I. Sánchez), [bram.vanginneken@radboudumc.nl](mailto:bram.vanginneken@radboudumc.nl) (B. van Ginneken).

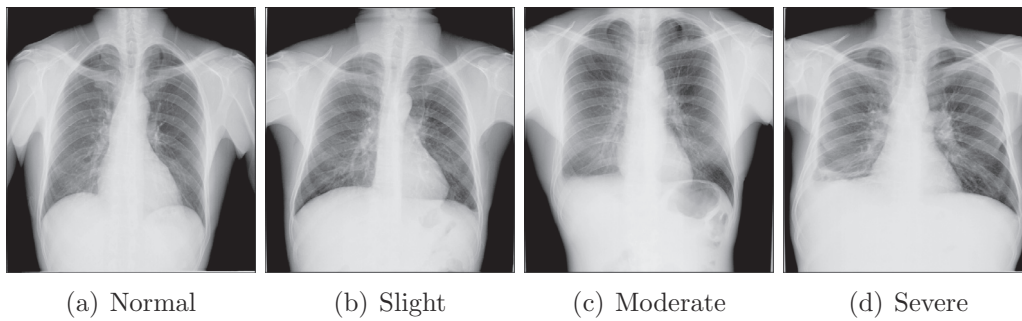


**Fig. 1.** Image categories as labeled by an experienced radiologist. (a) Completely normal image. (b) Left costophrenic recess with slight PE. (c) Right costophrenic recess with moderate PE. (d) Right costophrenic recess with severe PE.

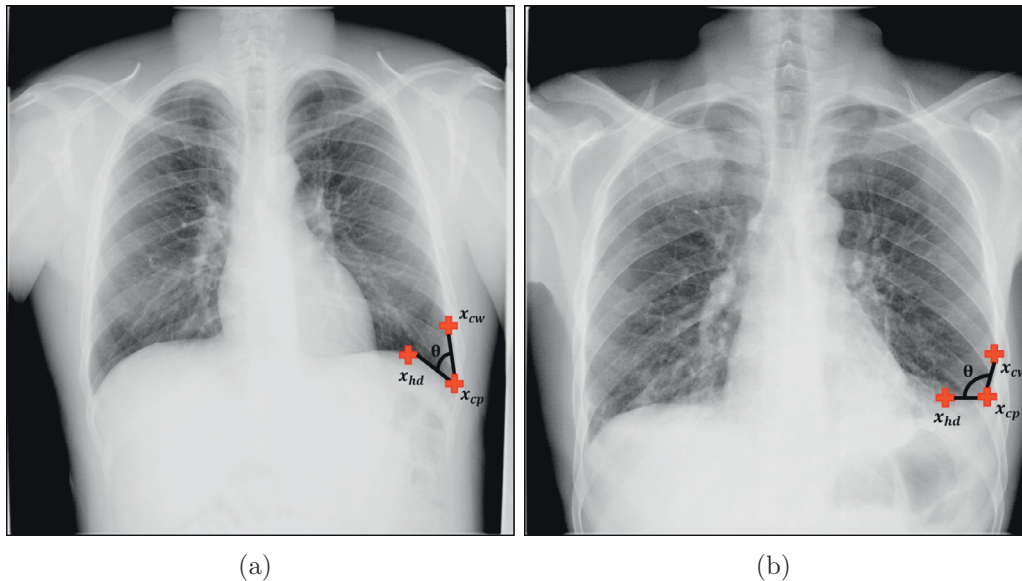


**Fig. 2.** Angle method proposed by Armato et al. (1998). (a) Normal CXR, (b) Abnormal CXR with a left blunt costophrenic angle.  $x_{cp}$ : costophrenic point,  $x_{hd}$ : hemi-diaphragm point,  $x_{cw}$ : chest wall point,  $\theta$  is the measured CP angle.

only abnormality present in the CXR. Limited research has been done on automatic detection of PE. Avni et al. (2011) proposed a “bag of visual words” approach to differentiate between various pathologies in CXRs including a small PE dataset of 17 and 21 images with right and left PE, respectively. In a recent work by Bar et al. (2015), a deep convolutional neural network was used to differentiate between various pathologies on 433 chest radiographs including 44 CXRs with right plural effusion. Armato et al. (1998) developed a dedicated method which uses automatic lung segmentation to measure the angle between the hemidiaphragm and lateral chest wall, commonly known as the CP angle, to identify the amount of PE in each hemithorax. Fig. 2 illustrates the CP angle for a normal and an abnormal CXR with PE in the left hemithorax. The presence of fluid causes bluntness of the CP angle, leading to a larger angle measurement in contrast to an acute angle as it would be seen in a normal CXR. In our preliminary work on PE detection (Maduskar et al. (2013)), we calculated the difference in distribution of angle measurements between normal and abnormal hemithoraces with PE, and found considerable overlap between the two distributions. We therefore concluded that although angle measurement by itself is insufficient, it is an important feature and its accurate calculation is critical for PE detection.

In this work, we propose a CAD system for PE detection with two novel aspects: 1. Robust localization of the CP recess by means of combined anatomical landmark information and local refinement of the lung segmentation, and 2. PE detection using CP region and angle analysis. We define the CP point as the point of intersection of the lateral chest wall and the diaphragm as shown in Fig. 2. Ac-

curate localization of the CP point is required for correct CP recess extraction and the angle measurement. In the previous approach by Armato et al. (1998), lung segmentation was used as the only structure for CP point extraction. In this work, in addition to the lung segmentation, the chest-wall is included as an additional structure for robust localization of the CP point. Further, the lung segmentation is refined in a local neighborhood around the detected CP point to obtain a more accurate angle measurement. In contrast to the previous work by Armato et al. (1998) where only the calculated angle was used to identify PE, our method also analyzes the region around the CP point. We introduce two region descriptors based on intensity and morphology information to improve PE identification. Results are reported on two separate systems trained to classify left and right hemithoraces, which is motivated by anatomical variation between left and right costophrenic recesses.

## 2. Data

The dataset used in this study was collected from two health centers in Lusaka, Zambia. The patients reporting to these clinics are TB suspects, i.e. they have clinical symptoms associated with TB. The CXRs were acquired using a digital Odelca-DR system with a slotscan detector (Delft Imaging Systems, The Netherlands) in the years 2009–2013 at a tube voltage ranging between 100–140 kVp adjusted per patient. The image resolution of the CXRs varied between 1560–2704 and 1520–2724 pixels in height and width, respectively, with a pixel spacing of 256x250  $\mu\text{m}$ . A human reader (a trained medical student)

**Table 1**

Overview of the dataset and the reference standard for the left and right hemithoraces for the training and test set.

Dataset		Normal (0)	Slight (1)	Moderate (2)	Severe (3)	Total #images (Hemithoraces)
Training	Left	491	61	37	40	629 (1258)
	Right	524	53	28	24	
Test	Left	495	57	41	45	638 (1276)
	Right	540	40	38	20	

went through 15,000 CXRs to identify CXRs containing PE. The human reader was encouraged to overread in case of doubt about the presence of pleural fluid. Images containing gross pathology were excluded from the study as such cases can be easily detected by conventional TB CAD systems (Hogeweg et al. (2015)). The reader identified 636 CXRs with potential pleural fluid. These 636 CXRs were re-read by a chest radiograph reading and recording system (CRRS) certified B reader (Dawson et al. (2010)) and 392 CXRs were confirmed as PE cases. 875 completely normal images, also confirmed by the CRRS reader, collected from the same database, were added to the 392 CXRs to form the dataset for this study. Following the above process, in total 1267 CXRs (2534 hemithoraces) were collected. These were subsequently read by a chest radiologist with over thirty years of experience to set the reference standard. The radiologist classified PE in each hemithorax in one of the 4 categories: 0 (Normal), 1 (Slight PE), 2 (Moderate PE) and 3 (Severe PE). We used the same categories as in Armato et al. (1998) to perform a comparison with the results achieved using only the angle measurement. Fig. 1 illustrates the four categories of PE. The CXRs were randomly divided into training and test set for training and evaluation of the PE detection system. An overview of the characteristics of the dataset and the reference standard determined by the radiologist is provided in Table 1.

### 3. Methods

The stages of the proposed PE detection method are summarized in Fig. 3. Firstly, two anatomical structures, the lung fields and the chest wall are detected, which are required for accurate localization of the CP point. Using these structures, the location of the CP point is calculated in two steps, the first step involves detection of the coarse location of the point followed by a refinement step. A region of interest around the CP point corresponding to the CP recess is extracted and three feature descriptors - angle, intensity and morphology, are measured to construct a feature vector. Finally, a supervised classification methodology is employed to assign an abnormality score to the feature vector indicating severity of PE.

The following subsections describe the procedure to detect PE in the left lung field (hemithorax). An equivalent approach is applied for the analysis of the right lung, after mirroring the image. Given the input image  $I$ , it is resized to a width of 1024 pixels for computational purposes. Resizing to a fixed resolution would be detrimental,

we take advantage of the fact that CXRs, if properly acquired, collimate the field of view to fit the thorax. We express all size parameters in pixels in these resized images, 1 pixel roughly corresponds to 0.4 mm. Moreover,  $I$  is downsampled to a width of 256 pixels before performing the lung segmentation and chest wall delineation for fast feature computation and classification.

#### 3.1. Lung segmentation

The lung fields can be used to locate the costophrenic recess. Lung segmentation is performed by applying a previously described segmentation method (van Ginneken et al. (2006)). The main difference between the published method and the one described here, is the training dataset. A much larger dataset consisting of 309 CXRs from two different sources is used: 200 from Lusaka, Zambia and 109 from Bagamoyo, Tanzania. The image  $I$  is first rescaled to a width of 256 pixels, let the rescaled image be  $I'$ . Given a pixel  $\mathbf{x} = (x, y)$  in  $I'$ , pixel texture features are extracted using the output of Gaussian derivative filtered images (Koenderink and van Doorn (1987)). Specifically, Gaussian derivatives up to second order at scales  $s = 2^i$  pixels ( $i = 0, 1, 2, 3$  and 4) are calculated. Using these features, the original intensity value  $I'(\mathbf{x})$  and spatial coordinates  $(x, y)$ , a 33 dimensional feature vector is constructed and fed into a  $k$ -nearest neighbor (kNN) classifier (Duda et al. (2001)) for pixel classification. The classifier is trained with 309 images, on which the lung fields were manually annotated by a CRRS certified B reader. After classification, a pixel probability map  $M_{lung}$  indicating the likelihood that the pixel belongs to the lung region is obtained:

$$M_{lung}(\mathbf{x}) = p(\mathbf{x} \in lung | \mathbf{x}) \quad (1)$$

A binary lung segmentation  $B_{lung}$  is then calculated as:

$$B_{lung}(\mathbf{x}) = \begin{cases} 1 & \text{if } M_{lung}(\mathbf{x}) * G(\mathbf{x}; \sigma) \geq 0.5 \\ 0 & \text{otherwise} \end{cases} \quad (2)$$

where  $G(\mathbf{x}; \sigma)$  is a Gaussian kernel with scale parameter  $\sigma$ , and  $*$  denotes the convolution operation. A threshold of 0.5 seemed to be an obvious choice to compute  $B_{lung}$  and has been previously used in literature (van Ginneken et al. (2006)). The scale parameter is set as  $\sigma = 1$  to slightly blur the probability map  $M_{lung}$  to reduce noise and inhomogeneities. Furthermore, the largest connected component is selected and hole filling is applied on  $B_{lung}$  to get the final segmentation  $B_{lung}$  (see Fig. 4(b) and (c)).

#### 3.2. Chest wall delineation

Lung segmentation is usually not sufficient to locate the CP point as  $B_{lung}$  can be inaccurate, for example because of the presence of abnormalities or a stomach bubble. We have found that the lateral chest wall, on the other hand, is always prominently visible due to the dense bright overlapping ribs that surround the lung region even in acutely diseased lungs. Consequently, we used the chest

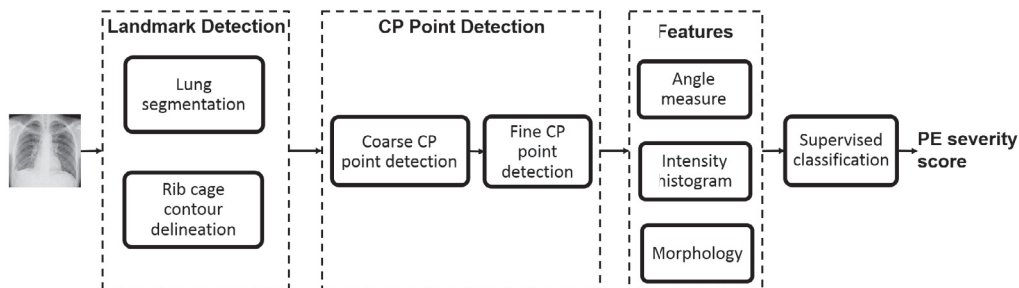


Fig. 3. Flowchart of the proposed method for automatic PE detection given an input image  $I$ .

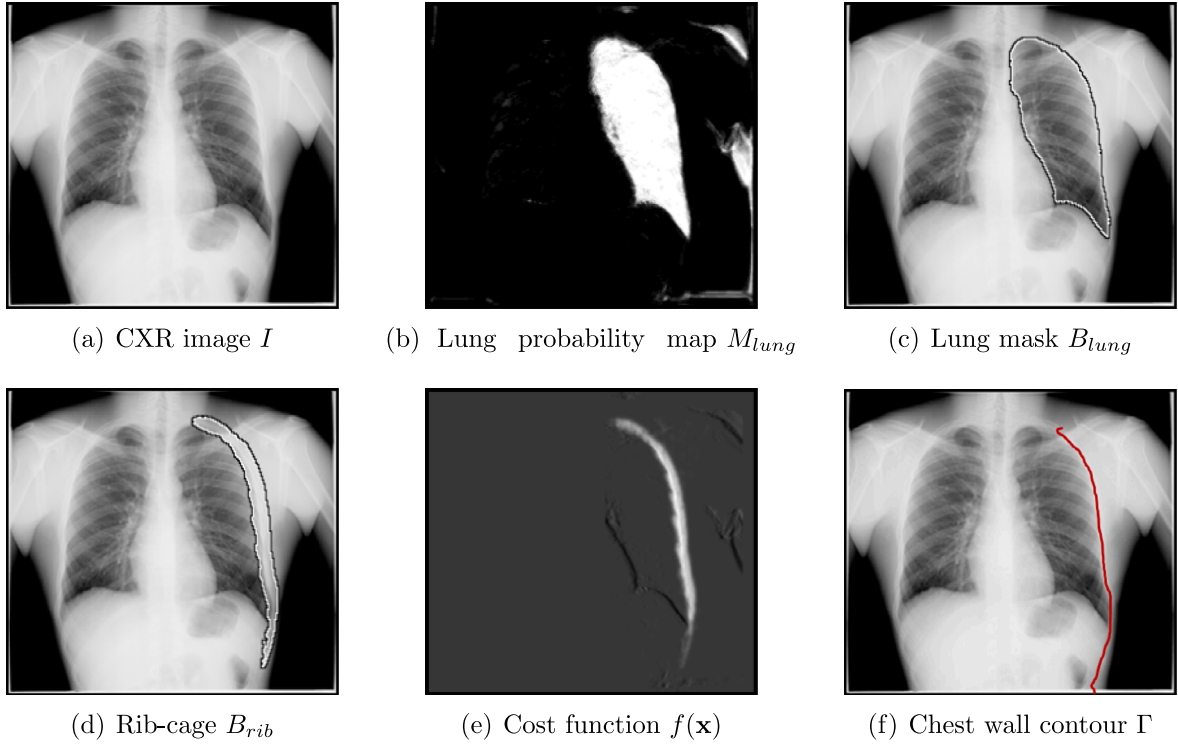


Fig. 4. Lung and rib cage segmentation, followed by chest wall contour delineation.

wall contour in conjunction with the lung segmentation to robustly detect the CP point.

To detect the lateral chest wall, the lateral rib cage is segmented first, which is followed by the extraction of the chest wall contour. Similar to the approach followed for lung segmentation, a feature vector for each pixel  $\mathbf{x} \in I'$  is constructed using the previously described texture features at scales - 1, 2, and 4 pixels, the original intensity value  $I'(\mathbf{x})$ , pixel spatial coordinates ( $x$  and  $y$ ) and two additional feature sets, namely a ridge feature and lung context features.

The lateral rib cage surrounding the lung can be viewed as a bright tubular structure which is captured by the ridgeness measure. The 2-D ridgeness measure is calculated using the two eigenvalues of the Hessian matrix at multiple scales (Lindeberg (1998)). Specifically, it is calculated at scales - 1, 2 and 4 pixels at each pixel  $\mathbf{x}$ , and the maximum value is assigned as the ridge feature value for each pixel  $\mathbf{x}$  in  $I'$ . The scales are appropriately chosen to capture the size of the rib cage in  $I'$ .

Lungs are encompassed by the rib cage and hence the lung fields are used as a guiding structure for the lateral rib-cage detection. Four lung contextual features are extracted using the binary lung segmentation  $B_{lung}$ . The features include normalized  $x$  and  $y$  positions relative to the lung bounding box around  $B_{lung}$ , distance to the lung wall and distance to the center of gravity of  $B_{lung}$ . These features aid in detecting only lateral rib cage, otherwise all the bony structures would get a high response if only texture and ridge features are used.

A  $k$ NN classifier ( $k=15$ ) is then used to classify the pixels in  $I'$  on the basis of the resulting feature vector consisting of 26 features. An independent set of 50 images originating from Lusaka, Zambia is used to train the classifier, where manually annotated pixels inside and outside the rib cage are sampled as the training set. The lateral rib cage in these CXRs were annotated by a CRRS certified B reader. After classification, a pixel probability map  $M_{rib}$  indicating the likelihood that the pixel belongs to the rib cage is obtained:

$$M_{rib}(\mathbf{x}) = p(\mathbf{x} \in ribcage | \mathbf{x}) \quad (3)$$

The binary rib cage segmentation  $B_{rib}$  is then calculated as:

$$B_{rib}(\mathbf{x}) = \begin{cases} 1 & \text{if } M_{rib}(\mathbf{x}) * G(\mathbf{x}; \sigma) \geq 0.1 \\ 0 & \text{otherwise} \end{cases} \quad (4)$$

where  $G(\mathbf{x}; \sigma)$  is a Gaussian kernel with scale parameter  $\sigma$  and  $*$  denotes the convolution operator. The scale parameter is set as 1 to smoothen the probability map  $M_{rib}$ . A low threshold of 0.1 is chosen on  $M_{rib}$  to oversegment the lateral rib-cage as it is used as a bounding box for calculating the chest wall contour.

Given  $B_{rib}$ , a dynamic programming approach is applied to compute an optimal path which begins at the start pixel coordinates of the bounding box around  $B_{rib}$  until the end of the image  $I$ . The cost associated with the path is calculated based on a local cost function  $f(\mathbf{x}) = M_{rib}(\mathbf{x}) + \frac{\partial M_{lung}(\mathbf{x})}{\partial x}$ . The first order derivative of  $M_{lung}$  along the  $x$  direction gives a high response on the lateral chest wall while suppressing the high response on the diaphragm. Hence, a cost function constructed using  $\frac{\partial M_{lung}(\mathbf{x})}{\partial x}$  will complement in case of a low rib posterior probability response  $M_{rib}$ .

The resulting maximum cost path corresponds to the chest wall contour  $\Gamma$ . Fig. 4(d)–(f) demonstrates the lateral rib-cage segmentation, the cost image and the chest wall delineation, respectively.

### 3.3. Coarse costophrenic point detection

Characteristics of the CP point suggest that it lies on the diaphragm and in proximity of the chest wall contour depending on the amount of fluid. Hence, we used the chest wall contour  $\Gamma$  and the lung probability map  $M_{lung}$  to detect the coarse location of the CP point. The principle behind detecting such a point is to identify a contour point on  $\Gamma$  in a predefined neighborhood at the junction of chest wall and diaphragm. We hypothesize that in the neighborhood of the CP point where the diaphragm intersects the chest wall contour, a maximum intensity variation is shown due to the transition from the lung to the background region. Following this approach, we

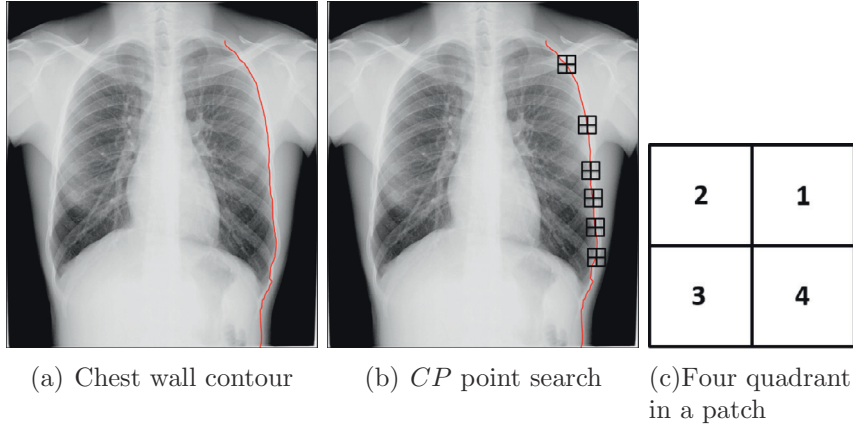


Fig. 5. Procedure for coarse CP point detection defined as  $\mathbf{x}_{ccp}$ .

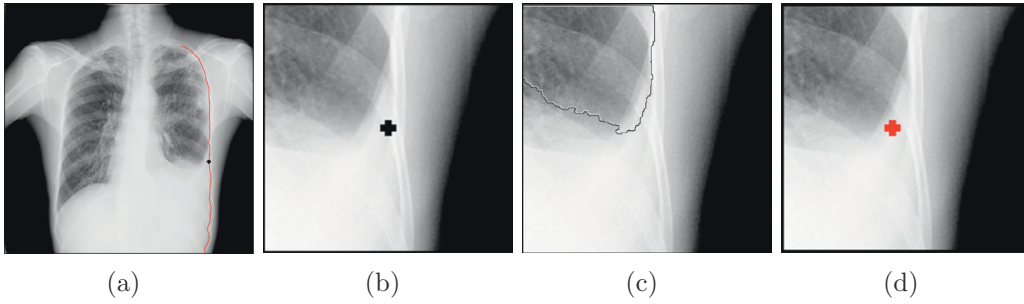


Fig. 6. Coarse ( $\mathbf{x}_{ccp}$ ) to fine ( $\mathbf{x}_{cp}$ ) CP point detection. (a) The chest wall contour  $\Gamma$  and  $\mathbf{x}_{ccp}$  overlaid on the CXR image  $I$ . (b) Subimage  $S$  around  $\mathbf{x}_{ccp}$ . (c) Overlaid lung component  $B_{lung}^S$  (Eq. 9) on  $S$ . (d) Refined CP point  $\mathbf{x}_{cp}$  indicated by the marker (Eq. 10).

analyze the neighborhood of each contour point in  $\Gamma$  as described hereafter.

For each  $\mathbf{x} \in \Gamma$ , a square region  $\Omega(\mathbf{x}, d)$  of size  $d$  centered at  $\mathbf{x}$  is defined. Let  $\Omega(\mathbf{x}, d)$  be divided in four quadrants  $\Omega_q(\mathbf{x}, d)$  with  $q = 1, 2, 3, 4$  as shown in Fig. 5(c). The coarse left CP point is calculated as the point with maximum difference between the mean pixel probability  $M_{rib}$  in the quadrants 2 and 3. If the coarse CP point  $\mathbf{x}_{ccp}$  is detected correctly, quadrant 3 would ideally have minimal or no lung pixels. The coarse CP point  $\mathbf{x}_{ccp}$  is identified as follows:

$$\mathbf{x}_{ccp} = \operatorname{argmax}_{\mathbf{x} \in \Gamma} [\mu_2(\mathbf{x}) - \mu_3(\mathbf{x})] \quad (5)$$

with

$$\mu_q(\mathbf{x}) = \frac{1}{N_q} \sum_{\mathbf{x}_j \in \Omega_q(\mathbf{x}, d)} M_{lung}(\mathbf{x}_j) \quad (6)$$

where  $N_q$  is the total number of pixels in  $\Omega_q(\mathbf{x}, d)$ .

The value of  $d$  is selected as 64 pixels such that sufficient lung and background pixels are included but the region is small enough to perform the local analysis around the chest wall. Fig. 5(a) and (b) illustrates the process of coarse CP point detection.

### 3.4. Fine costophrenic point detection

The method described in the previous section provides a coarse location  $\mathbf{x}_{ccp}$  of the CP point as the point is constrained to be on the chest wall. Localization of  $\mathbf{x}_{ccp}$  is accurate for normal CXRs but if fluid is present, the actual CP point does not strictly lie on the contour. As a consequence, we need to refine the location of the CP point which takes  $\mathbf{x}_{ccp}$  as an input. We therefore extract a subimage  $S = S(\mathbf{x}_{ccp}, w)$  of  $I$  centered at  $(x_{ccp}, y_{ccp})$  with size  $w$ , to improve the location of the CP point, by locally refining the lung segmentation in the subimage. Based on experimentation, we chose  $w$  as 256 pixels to include sufficient lung region and background for the local lung refinement as described in further steps.

Let  $M_{lung}^S$  be the corresponding lung probability map ( $M_{lung}$ ) of  $S$ . For each pixel  $\mathbf{x} \in S$ , we calculate three values, namely the lung probability value  $M_{lung}^S(\mathbf{x})$  and the spatial relative coordinates of  $\mathbf{x}$  in  $S$ . Based on these values,  $S$  is divided into three distinct regions  $R_k$  with  $k = 1, 2, 3$  using  $k$ NN clustering algorithm (Duda et al. (2001)). These regions correspond to the lung area, background, and other regions containing spurious edges or artifacts.

A binary segmentation  $B^S$  of  $S$  is then obtained as follows:

$$B^S(\mathbf{x}) = \begin{cases} 1 & \text{if } \mathbf{x} \in R_{k^*} \\ 0 & \text{if } \mathbf{x} \in R_k, \forall k \neq k^* \end{cases} \quad (7)$$

with

$$k^* = \operatorname{argmax}_k \frac{1}{N_k} \sum_{\mathbf{x}_j \in R_k} M_{lung}^S(\mathbf{x}_j) \quad (8)$$

where  $N_k$  is the total number of pixels in  $R_k$ .

This binary segmentation  $B^S$  can contain one or more connected components  $C_m$ , with  $m \geq 1$ , including the lung region and other objects, such as the stomach bubble if visible. The final refined lung segmentation  $B_{lung}^S$  in  $S$  is calculated as:

$$B_{lung}^S(\mathbf{x}) = \begin{cases} 1 & \text{if } \mathbf{x} \in C_{m^*} \\ 0 & \text{if } \mathbf{x} \in C_m, \forall m \neq m^* \end{cases} \quad (9)$$

with  $m^* = \operatorname{argmin}_m \|\mathbf{x}_{g,m}\|$  and  $\mathbf{x}_{g,m}$  the center of gravity of  $C_m$ .

The CP point location  $\mathbf{x}_{cp}^S$  is calculated as the pixel in the refined lung segmentation  $B_{lung}^S$  with a maximum distance to the contralateral upper corner of  $B_{lung}^S$ . Therefore,  $\mathbf{x}_{cp}^S$  in  $S$  is then defined as:

$$\mathbf{x}_{cp}^S = \operatorname{argmax}_{\substack{\mathbf{x} \in S \\ B_{lung}^S(\mathbf{x})=1}} \|\mathbf{x}\| \quad (10)$$

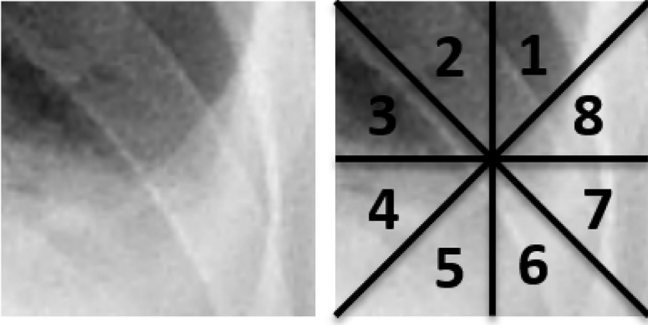


Fig. 7. Intensity features: Illustration of 8 regions used for histogram computation.

and the CP point location in  $I$  is:

$$\mathbf{x}_{cp} = (x_{cp}, y_{cp}) = \left( x_{cp}^s + x_{ccp} - \frac{w}{2}, y_{cp}^s + y_{ccp} - \frac{w}{2} \right) \quad (11)$$

### 3.5. Features

Given the CP point  $\mathbf{x}_{cp}$ , several features are extracted to identify PE. These features can be broadly divided into three categories: angle, intensity and morphology features. The angle measurement is highly dependent on the location of  $\mathbf{x}_{cp}$  and the points chosen on the chest wall and the hemidiaphragm. Following this observation, we have introduced new features as explained in the subsequent sections.

#### 3.5.1. Angle

The angle measurement  $\theta$  is calculated as described in [Armato et al. \(1998\)](#). We use the refined lung segmentation  $B_{lung}^S$  (see [Section 3.4](#)) to localize the “chest wall point” ( $\mathbf{x}_{cw}$ ) and the “hemidiaphragm point” ( $\mathbf{x}_{hd}$ ) (see [Fig. 2](#)). The lung contour pixels are determined as follows: if one or more 4-connected neighboring pixels of the foreground pixel ( $B_{lung}^S = 1$ ) belongs to the background ( $B_{lung}^S = 0$ ), the pixel under analysis is labeled as a lung contour pixel. The calculated lung contour is then traced starting from the CP point ( $\mathbf{x}_{cp}^s$ ) along the chest wall and the hemidiaphragm. We label the  $p^{th}$  pixel location on the chest wall and the hemidiaphragm as  $\mathbf{x}_{cw}$  and  $\mathbf{x}_{hd}$ , respectively. The CP angle is calculated between the two lines defined by a line joining these points ([Fig. 2](#)). Empirically,  $p = 40$  pixels is chosen for the angle measurement based on visual analysis of the angle measurements on the training data to ensure that the point is suitably placed to capture subtle bluntness.

#### 3.5.2. Intensity

Intensity features are computed to incorporate local intensity variation in the region around the CP point. For example, if we analyze an abnormal region with PE in the lung fields, the intensity values are higher than the normal lung parenchyma due to the presence of fluid. We capture these details using histogram analysis in various subregions around the CP point  $\mathbf{x}_{cp}$ . Let  $\Phi = \Phi(\mathbf{x}_{cp}, n)$  be a square patch of size  $n$  centered at  $\mathbf{x}_{cp}$  extracted from the image  $I$  and divided into 8 regions as shown in [Fig. 7](#). For each region, the intensity histogram is calculated with 5 equally sized bins between minimum and maximum intensity value in the patch. Note that the patch intensity values are normalized to zero mean and unit standard deviation before calculation. Histograms of the 8 regions are concatenated to form a feature vector. In total, the feature vector contained 40 (8 regions  $\times$  5 bins) intensity based features. We chose  $n = 64$  pixels for computation of the intensity features based on the performance in cross-validation experiments on the training dataset.

#### 3.5.3. Region morphology

The shape of the lung fields in the neighborhood of the CP point can provide an indication regarding the presence of pleural fluid. In

Table 2

Summary of the parameters used in various steps of the PE detection algorithm.

Algorithm step	Parameters
Lung Segmentation	$k = 15, \text{threshold} = 0.5, \sigma = 1$
Chest wall delineation	$k = 15, \text{threshold} = 0.1, \sigma = 1$
CP point detection	$d = 64, w = 256$
Angle measurement	$p = 40$
Intensity	$n = 64, \text{Number of regions} = 8, \text{Bin size} = 5$
Classification	$\text{Number of trees} = 500, \text{Depth} = 10$

case of a normal CP recess, the CP angle is usually sharp leading to less pixels belonging to the lung region ( $B_{lung}^S = 1$ ) and as a result the lung area is smaller in a normal region as compared to a region containing pleural fluid. This property is exploited using the refined lung segmentation  $B_{lung}^S$  ([Section 3.4](#)). Two features are calculated: 1. compactness, defined as  $\frac{4\pi N_l}{N_c^2}$ , where  $N_l$  is the number of lung pixels in  $S$  ( $B_{lung}^S = 1$ ) and  $N_c$  is the number of lung contour pixels of  $B_{lung}^S$ , and 2. the ratio of number of lung and background pixels,  $\frac{N_l}{N_b}$ , where  $N_b$  is the number of background pixels in  $S$  ( $B_{lung}^S = 0$ ).

### 3.6. Classification

Angle, patch and region morphology features are combined to form a feature vector of 43 descriptive features. A random forest (RF) classifier ([Breiman \(2001\)](#)) is trained with the feature vectors of normal (491) and abnormal (138) hemithoraces for the left PE detection. The number of trees and the maximum depth parameters are optimized by splitting the training set into training and validation set with an equal proportion of normals and abnormal. The parameters which resulted in maximum area under the receiver operating characteristic (ROC) curve on the validation set (half of the training set) are selected. The RF classifier is then retrained with the complete training dataset using the chosen parameters (number of trees:500, maximum depth:10).

[Table 2](#) provides a summary of the parameters used in each step of the proposed PE detection algorithm [Fig. 3](#).

## 4. Experiments and results

### 4.1. CP point localization accuracy

Identifying the correct CP point is crucial for the accuracy of the PE detection method. All the features, i.e. angle measurement, patch and morphology features are dependent on the location of CP point. Therefore, we compared the location of the automatically identified CP point with a manually indicated point. A CRRS certified B reader trained in reading CXRs for TB analyzed all the CXRs in the test set. Left and right CP points were marked at the point of intersection of the chest wall and the hemidiaphragm if clearly visible, otherwise, the reader was instructed to mark the point in the center of the costophrenic recess.  $L^2$  distance between the manually indicated point and the automatically detected CP point  $\mathbf{x}_{cp}$  was calculated. Additionally, we computed the distance between the manually indicated CP point and the CP point calculated using only the lung segmentation  $B_{lung}$  similar to the method described in [Armato et al. \(1998\)](#), where the CP point for each lung was identified as the most distant lung pixel ( $B_{lung} = 1$ ) from the contralateral upper corner of the CXR image. We denote the CP points calculated manually and using the original lung segmentation  $B_{lung}$  only, as  $\mathbf{x}_{cp, manual}$  and  $\mathbf{x}_{cp, lung}$ , respectively. Paired t-tests were used to evaluate significant differences for  $L^2$  distances between  $\mathbf{x}_{cp, manual}$  and  $\mathbf{x}_{cp, lung}$ , and  $\mathbf{x}_{cp, manual}$  and  $\mathbf{x}_{cp}$ .

An example image with the three CP points  $\mathbf{x}_{cp, manual}$ ,  $\mathbf{x}_{cp, lung}$ , and  $\mathbf{x}_{cp}$  for the left lung is shown in [Fig. 8](#). Note that the CP point

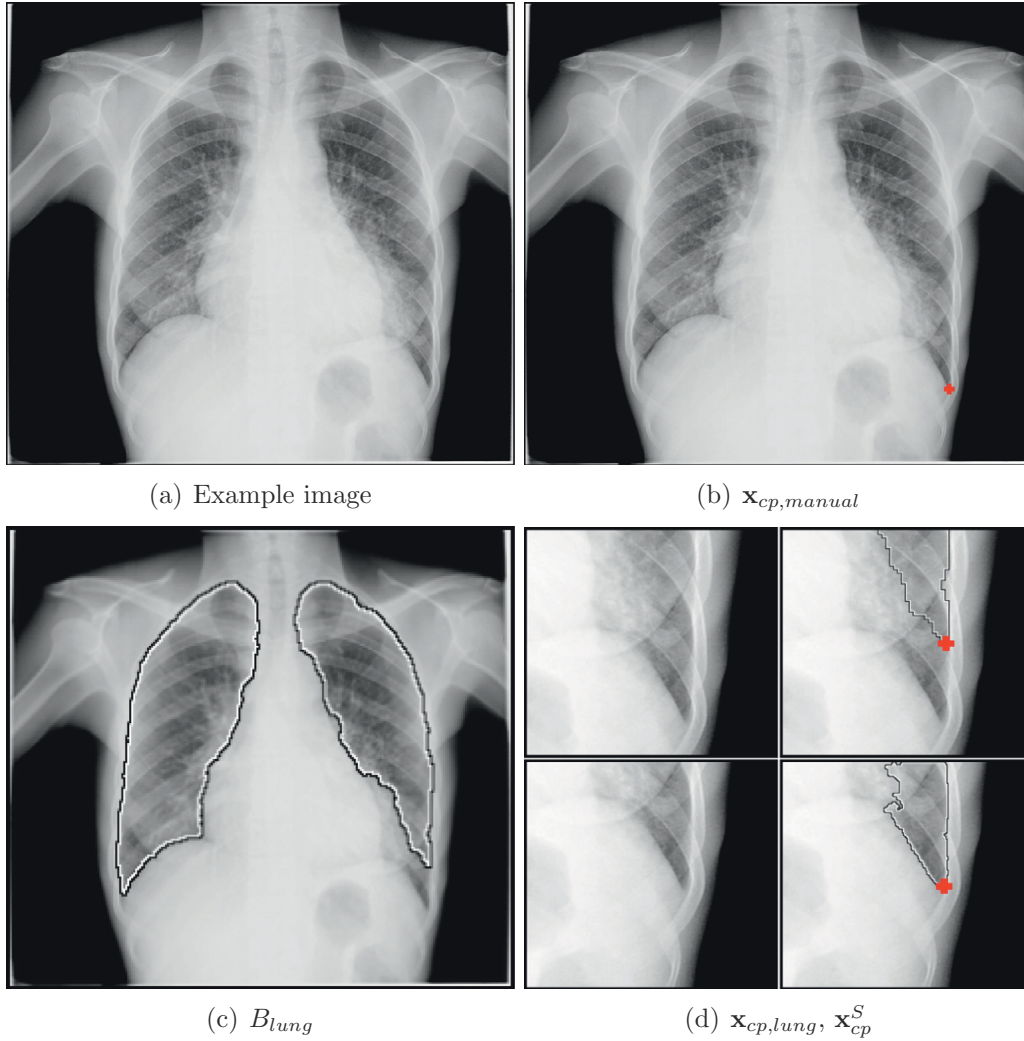


**Fig. 8.** Costophrenic point detection for various methods. (a) Example image. (b)  $\mathbf{x}_{cp,manual}$  indicated manually by a trained CXR reader. (c) Segmented lungs,  $B_{lung}$ . (d) The top row shows the subimage around  $\mathbf{x}_{cp,lung}$  (left) and the overlaid lung segmentation  $B_{lung}$  and  $\mathbf{x}_{cp,lung}$  plotted by a marker (right). The bottom row shows the subimage  $S$  (left) and the overlaid refined lung segmentation  $B_{lung}^S$  and the refined CP point  $\mathbf{x}_{cp}^S$  (right).

$\mathbf{x}_{cp,lung}$  is dislocated due to an incorrect lung segmentation, but is correctly identified by the newly proposed method ( $\mathbf{x}_{cp}$ ). Fig. 9 shows the box plots for the  $L^2$  distances between  $\mathbf{x}_{cp,manual}$  and  $\mathbf{x}_{cp,lung}$ , and  $\mathbf{x}_{cp,manual}$  and  $\mathbf{x}_{cp}$  for the left and right CP points. For the left CP point, the distances for  $\mathbf{x}_{cp,lung}$  and  $\mathbf{x}_{cp}$  to the manual reference were  $31.99 \pm 37.19$  pixels and  $30.71 \pm 36.87$  pixels ( $p = 0.04$ ) respectively, and  $20.00 \pm 23.69$  and  $18.07 \pm 22.47$  ( $p = 0.002$ ), for the right CP point, respectively.

#### 4.2. PE detection performance analysis

The performance of the proposed PE detection system was analyzed and compared in terms of area (AUC) under the ROC curve. ROC curves for the following three systems were compared - *System 1*: Angle feature computed using  $\mathbf{x}_{cp,lung}$  and  $B_{lung}$ . *System 2*: Angle feature computed using  $\mathbf{x}_{cp}$  and  $B_{lung}$  as mentioned in Section 3.5.1. *System 3*: The final PE abnormality score computed by the proposed method as described in Section 3.6. AUC of ROC curves for left and right PE detection were compared between the three systems. Significant differences were determined with case-based bootstrapping by calculating pair-wise differences of AUC values using 5000 bootstrap samples (Efron (1979)). Cases were resampled with replacement 5000 times and every bootstrap sample had the same number of cases as the

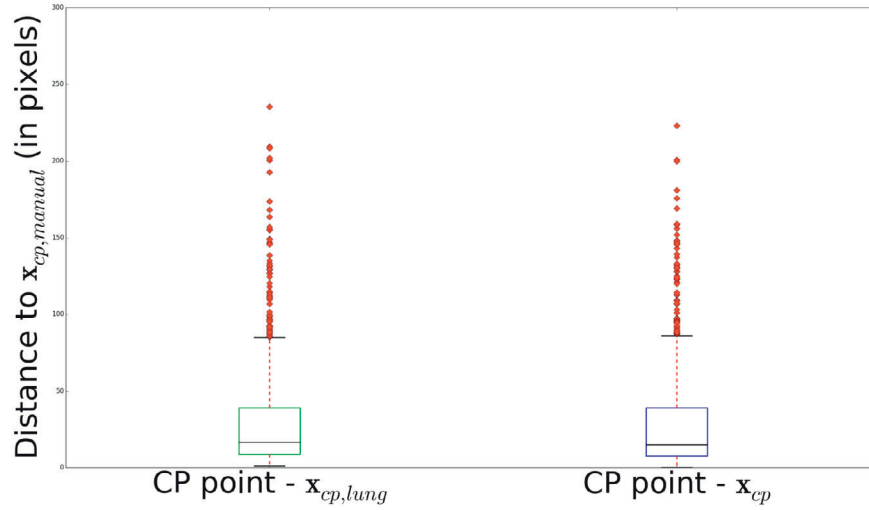
**Table 3**

AUC values with 95% confidence intervals for various PE detection systems. *System 1*: Angle feature computed using  $\mathbf{x}_{cp,lung}$  and  $B_{lung}$ . *System 2*: Angle feature computed using  $\mathbf{x}_{cp}$  and  $B_{lung}$ . *System 3*: Proposed PE detection system in this paper. \* indicates that *System 3* is significantly better than *System 1* and *System 2* ( $p < 0.0002$ ). CI: confidence interval.

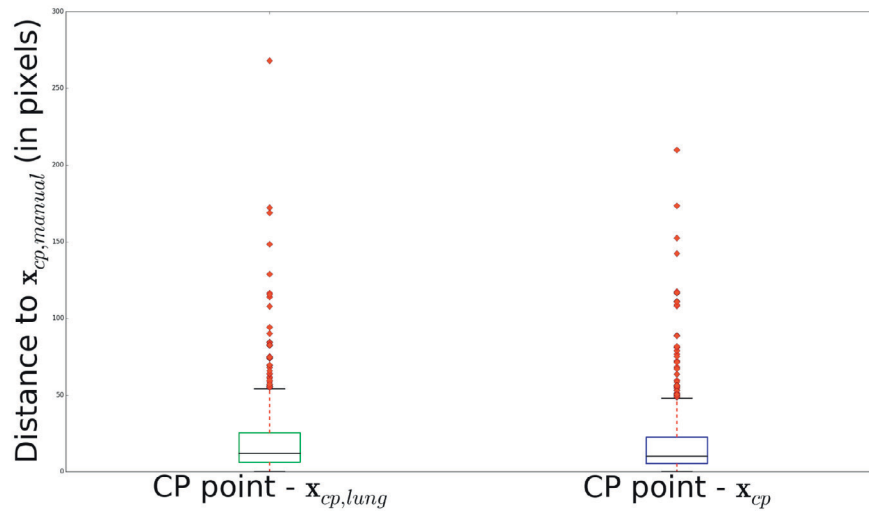
AUC [95% CI]	System 1	System 2	System 3 (Proposed)
Left	0.75 [0.71–0.80]	0.78 [0.73–0.82]	0.84 [0.80–0.87]*
Right	0.73 [0.68–0.79]	0.82 [0.77–0.87]	0.90 [0.87–0.93]*

original dataset. For each bootstrap sample, two ROC curves corresponding to the two systems being compared were constructed. The difference in AUC ( $\Delta AUC$ ) was computed, i.e. 5000 values of  $\Delta AUC$  were obtained.  $p$ -values were defined as the fraction of  $\Delta AUC$  values that were negative or zero (Samuelson and Petrick (2006)). Negative or zero differences in the AUC values between the systems under consideration will contribute to a higher  $p$ -value. Therefore, a  $p$ -value less than 0.05 was considered as a significant difference between the two ROC curves under comparison.  $p$ -values were calculated in pairs for *System 3* with *System 1* and *System 2*.

ROC curves and AUC values of the three systems for the left and right PE detection are shown in Fig. 10 and Table 3. The proposed PE

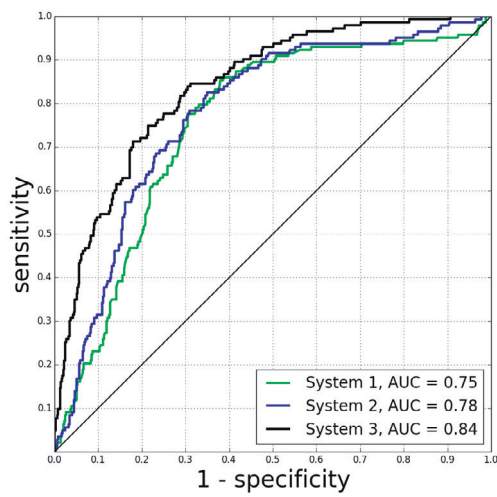


(a) Left costophrenic point

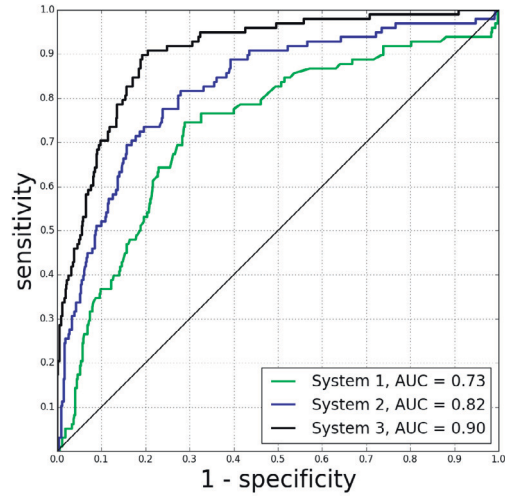


(b) Right costophrenic point

Fig. 9. Box plots for the distance between the manually indicated point  $x_{cp,manual}$  and the automatic methods ( $x_{cp,lung}$ ,  $x_{cp}$ ) on the test set.



(a) Left pleural effusion



(b) Right pleural effusion

Fig. 10. ROC curves for left and right pleural effusion detection. The ROC curve of System 3 (proposed system) is compared with System 1 and 2 as described in Section 4.2.

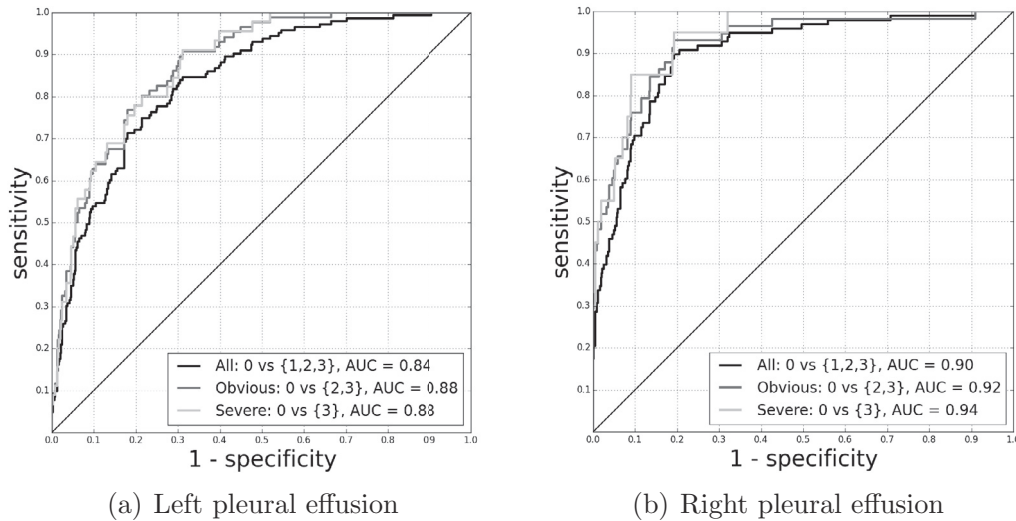


**Fig. 11.** ROC curves for left and right pleural effusion detection. The ROC curves are compared for the proposed method between the following three categories: All (0 vs {1, 2, 3}), Obvious (0 vs {2, 3}), Severe (0 vs {4}).

detection method (*System 3*) for both left and right hemithoraces performs significantly better than *System 1* and *System 2* ( $p < 0.0002$ ). *System 3* achieved sensitivities of  $\approx 83\%$  and  $\approx 72\%$  at 70% and 80% specificities, respectively, for the left PE detection, whereas higher sensitivities of  $\approx 92\%$  and  $\approx 90\%$  were observed at 70% and 80% specificities for the right PE detection.

#### 4.3. Subtlety based analysis

Subtlety based analysis was performed to analyze the results for different categories of PE (see [Table 1](#)). Consequently, ROC curves were computed for *System 3* by combining the following categories: All (0 vs {1, 2, 3}), Obvious (0 vs {2, 3}), Severe (0 vs {3}). While constructing the ROCs, hemithoraces with subtleties not under analysis were removed.

[Fig. 11](#) shows the ROC curves for all, obvious and severe PE vs normal CXRs for left and right PE detection systems. Higher values of AUC were observed for severe ( $AUC_{left}=0.88$  [0.83–0.92],  $AUC_{right}=0.94$  [0.90–0.98]) and obvious ( $AUC_{left}=0.88$  [0.84–0.91],  $AUC_{right}=0.92$  [0.88–0.96]) PE cases than for all cases ( $AUC_{left}=0.84$  [0.80–0.87],  $AUC_{right}=0.90$  [0.87–0.93]).

## 5. Discussion

The proposed PE detection system shows promising results for both left and right hemithoraces. The method uses a refined lung segmentation and chest wall contour to localize the CP point and this results in significantly higher accuracy compared to using the lung segmentation alone for the left CP point. The identification of the right CP point also showed significant improvement but not with a substantial difference ( $20.00 \pm 23.69$  vs  $18.07 \pm 22.47$  pixels) as compared to a large performance gain in the AUC values. Overall, the right CP point localization was better compared to the left CP point (see [Fig. 9](#)). This can be explained by the fact that complex anatomical structures are often present below the left lung, i.e. a stomach bubble, which makes the CP point detection harder in the left lung. When we compare the two CP localization techniques, the difference between the distances to the manually located CP points is small. Although, the differences are  $< 2$  pixels, it could lead to an incorrect angle measurement and calculation of the new proposed features in a wrong region, especially in case of subtle PE.

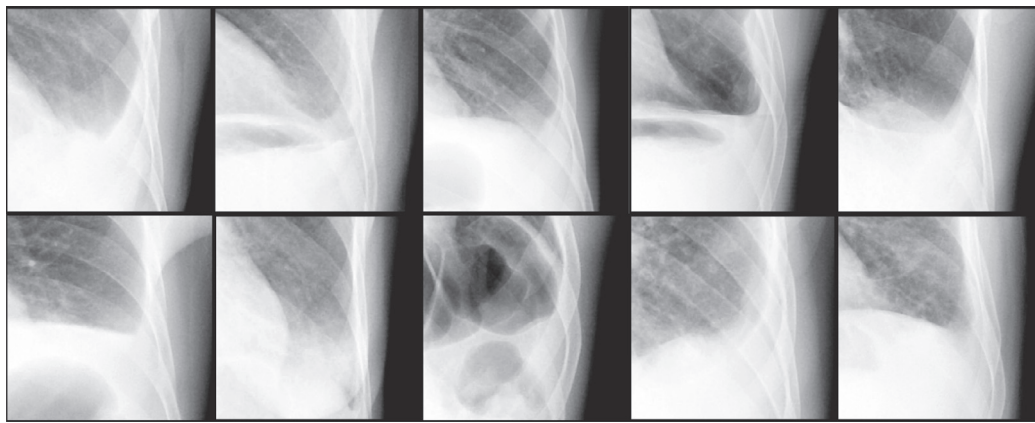
The proposed approach is compared to the simplified detection systems (*System 1* and *System 2*) using ROC analysis per lung. *System*

1 is implemented in a similar way as described in [Armato et al. \(1998\)](#) where we use the automatic lung segmentation to perform angle measurement. *System 2* uses the refined lung segmentation for the angle measurement and gives superior results as compared to *System 1*. *System 3* includes additional feature descriptors and the angle measurement of *System 2*, and exhibits significantly improved results compared to using only the angle measurement. The ROC curves in [Fig. 10](#) illustrate the superior results achieved by *System 3* for both left and right PE detection systems. These results demonstrate the advantage of additional feature descriptors and supervised classification over the angle based approach.

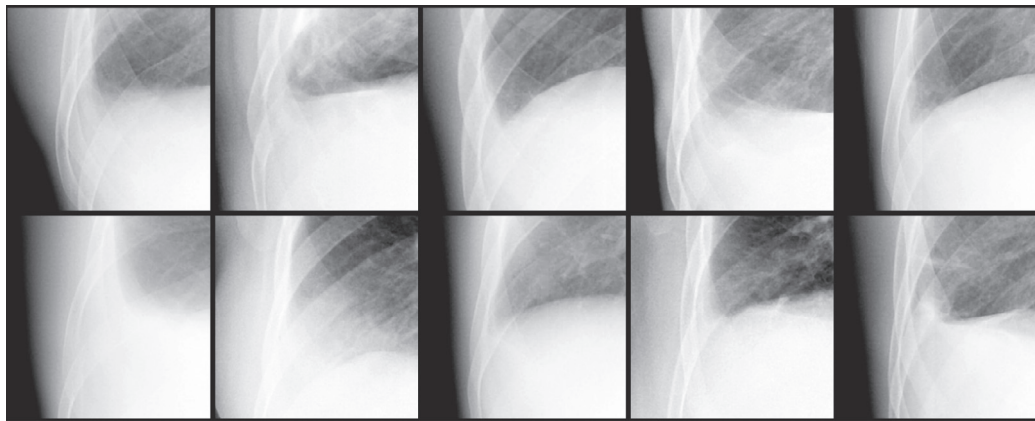
We have analyzed the results for different categories of PE and compared them with the results published in [Armato et al. \(1998\)](#). [Armato et al. \(1998\)](#) reported 0.75, 0.78 and 0.83 AUC values on 1116 hemithoraces for “All”, “Obvious” and “Severe” categories, respectively. The AUC values achieved in this work are higher for each category (see [Section 4.3](#)). Notably, the dataset used in the two studies is different but the AUC values obtained using *System 1* (0.75 and 0.73) are comparable to 0.75 in [Armato et al. \(1998\)](#). Hence, it can be reasoned that improved performance will be obtained on the dataset in [Armato et al. \(1998\)](#) using our approach. In addition, increased AUC values are observed using our method in case of “Severe” and “Obvious” PEs as compared to all PEs.

The highest ranked left and right subimages are shown in [Fig. 12](#). Eight out of ten top ranked images by the left PE detection system belong to “Severe” or “Moderate” PE categories. One image was wrongly classified as PE with a high abnormality score due to the presence of a stomach bubble, which resulted in a wrong lung segmentation and CP point location. The results reconfirm that PE detection is a harder task for the left lung than for the right lung. The top ten results of the right PE detection system are all true positive with two “Severe” and eight “Moderate” PE subimages (see [Fig. 12\(b\)](#)).

The presented work has a few limitations. In rare cases PE does not manifest in the CP recess but only along the chest wall or a pulmonary fissure, and such cases will not be detected by the proposed system. The system does not perform well on cases containing subtle PEs. Majority of the lowest scoring PE subimages in [Fig. 13](#) belong to “Slight” category and are not detected by the system. Assessing the presence of subtle PE is highly subjective, therefore an observer study comparing the performance of a human expert on these cases against the reference standard could be useful to investigate the inter-reader variability. A human reader could use the automatic PE detection system as an aided tool to detect subtle PE cases, but the



(a) Left PE subimages



(b) Right PE subimages

**Fig. 12.** The top ten ranked PE subimages by the left (a) and right (b) PE detection systems. The subimages are arranged in the highest to lowest order of abnormality scores. .



(a) Left PE subimages



(b) Right PE subimages

**Fig. 13.** Five lowest scored left (a) and right (b) PE subimages. The subimages are arranged in the lowest to highest order of abnormality scores.

performance of a human observer with and without the CAD system still needs to be evaluated in a future observer study. The results presented in this work were evaluated for statistical significance and not clinical relevance (Bhardwaj et al. (2004)). A validation study should be performed to evaluate the clinical relevance by measuring the final outcome in terms of number of additional TB cases detected by using a PE detection system in conjunction with symptoms or other CAD systems for TB.

CXRs with gross abnormalities were not included in this study. CXRs containing PE and gross parenchymal abnormalities near the lung bases might not be detected by the proposed system. In such cases, usually the lungs could be under-segmented leading to extraction of inaccurate region of interest for PE analysis. The proposed approach tries to rectify this issue by introducing a robust way of CP point detection using the chest wall and refined lung region.

A dedicated PE detection system such as the one proposed in this paper can be used in two scenarios. First, it can be used independently for the detection of accumulated fluid in the pleura which could be used to assess prognosis of not only TB but also other diseases, for example, cancer, heart failure and pneumonia (Porcel et al. (2014)). Second, the system can also be combined with an existing CAD program to detect PE in addition to parenchymal abnormalities. This will make the CAD system robust in the cases where PE is the only abnormality present in the CXR. Future work would include improving the PE detection system specifically for the left lung, and evaluating a full TB CAD system with inclusion of the proposed system.

## 6. Conclusions

A fully automatic method for the detection of pleural effusion on chest radiographs was presented. The method was evaluated on a tuberculosis dataset of 1276 hemithoraces containing 241 hemithoraces with pleural effusion. AUC values of 0.84 and 0.90 were achieved for the left and right hemithoraces, respectively. These results are superior to prior work where only the costophrenic angle was used to assess the presence of PE.

## Acknowledgments

This research was supported by the [European and Developing Countries Clinical Trials Partnership \(EDCTP\) grant \(TB-NEAT; IP.2009.32040.009\)](#): the Evaluation of multiple novel and emerging technologies for TB diagnosis, in smear-negative and HIV-infected persons, in high burden countries (TB-NEAT project). The content of this manuscript is solely the responsibility of the authors and the funding body had no role in the decision to publish or preparation of the manuscript.

## References

- Armato, S.G., Giger, M.L., MacMahon, H., 1998. Computerized delineation and analysis of costophrenic angles in digital chest radiographs. *Acad. Radiol.* 5, 329–335.
- Avni, U., Greenspan, H., Konen, E., Sharon, M., Goldberger, J., 2011. X-ray categorization and retrieval on the organ and pathology level, using patch-based visual words. *IEEE Trans. Med. Imaging* 30, 733–746. doi:10.1109/TMI.2010.2095026.
- Bar, Y., Diamant, I., Wolf, L., Lieberman, S., Konen, E., Greenspan, H., 2015. Chest pathology detection using deep learning with non-medical training. In: *IEEE International Symposium on Biomedical Imaging*, pp. 294–297. doi:10.1109/ISBI.2015.7163871.
- Baumann, M.H., Nolan, R., Petrini, M., Lee, Y.C.G., Light, R.W., Schneider, E., 2007. Pleural tuberculosis in the United States: incidence and drug resistance. *Chest* 131, 1125–1132. doi:10.1378/chest.06-2352.
- Bhardwaj, S.S., Camacho, F., Derrero, A., Fleischer Jr., A.B., Feldman, S.R., 2004. Statistical significance and clinical relevance: the importance of power in clinical trials in dermatology. *Arch. Dermatol.* 140 (12), 1520–1523. doi:10.1001/archderm.140.12.1520.
- Breiman, L., 2001. Random forests. *Mach. Learn.* 45, 5–32.
- Dawson, R., Masuka, P., Edwards, D.J., Bateman, E.D., Bekker, L.-G., Wood, R., Lawn, S.D., 2010. Chest radiograph reading and recording system: evaluation for tuberculosis screening in patients with advanced HIV. *Int. J. Tuberc. Lung Dis.* 14, 52–58.
- Duda, R.O., Hart, P.E., Stork, D.G., 2001. *Pattern Classification*, second John Wiley and Sons, New York.
- Efron, B., 1979. Bootstrap methods: Another look at the jackknife. *Ann. Stat.* 7, 1–26.
- Giger, M.L., Karssemeijer, N., Armato, S.G., 2001. Computer-aided diagnosis in medical imaging. *IEEE Trans. Med. Imaging* 20, 1205–1208.
- van Ginneken, B., Stegmann, M.B., Loog, M., 2006. Segmentation of anatomical structures in chest radiographs using supervised methods: a comparative study on a public database. *Med. Image Anal.* 10, 19–40. doi:10.1016/j.media.2005.02.002.
- Hogeweg, L., Mol, C., de Jong, P.A., Dawson, R., Ayles, H., van Ginneken, B., 2010. Fusion of local and global detection systems to detect tuberculosis in chest radiographs. In: *Medical Image Computing and Computer-Assisted Intervention*. In: *Lecture Notes in Computer Science*, 6363, pp. 650–657. doi:10.1007/978-3-642-15711-0\_81.
- Hogeweg, L., Sánchez, C.I., Maduskar, P., Philipsen, R., Story, A., Dawson, R., Theron, G., Dheda, K., Peters-Bax, L., van Ginneken, B., 2015. Automatic detection of tuberculosis in chest radiographs using a combination of textural, focal, and shape abnormality analysis. *IEEE Trans. Med. Imaging* 34, 2429–2442. doi:10.1109/TMI.2015.2405761.
- van't Hoog, A.H., Langendam, M.W., Mitchell, E., Cobelens, F.G., Sinclair, D., Leeftang, M.M.G., Lonnroth, K., 2013. A systematic review of the sensitivity and specificity of symptom- and chest-radiography screening for active pulmonary tuberculosis in HIV-negative persons and persons with unknown HIV status. Report to WHO.
- Jaeger, S., Karargyris, A., Candemir, S., Folio, L., Siegelman, J., Callaghan, F., Xue, Z., Palaniappan, K., Singh, R., Antani, S., 2013a. Automatic tuberculosis screening using chest radiographs. *IEEE Trans. Med. Imaging* 33, 233–245. doi:10.1109/TMI.2013.2284099.
- Jaeger, S., Karargyris, A., Candemir, S., Siegelman, J., Folio, L., Antani, S., Thoma, G., 2013b. Automatic screening for tuberculosis in chest radiographs: a survey. *Quant. Imaging Med. Surg.* 3, 89.
- Koenderink, J.J., van Doorn, A.J., 1987. Representation of local geometry in the visual system. *Biol. Cybern.* 55, 367–375.
- Koeslag, A., de Jager, G., 2001. Computer aided diagnosis of miliary tuberculosis. In: *Proceedings of the Pattern Recognition Association of South Africa*.
- Liam, C.K., Lim, K.H., Wong, C.M., 2000. Causes of pleural exudates in a region with a high incidence of tuberculosis. *Respirology* 5, 33–38.
- Lindeberg, T., 1998. Feature detection with automatic scale selection. *Int. J. Comput. Vis.* 30, 79–116.
- Maduskar, P., Hogeweg, L., Philipsen, R., van Ginneken, B., 2013. Automated localization of costophrenic recesses and costophrenic angle measurement on frontal chest radiographs. In: *Medical Imaging*. In: *Proceedings of the SPIE*, 8670, p. 867038. doi:10.1117/12.2008239.
- Muyoyeta, M., Maduskar, P., Moyo, M., Kasese, N., Milimo, D., Spooner, R., Kapata, N., Hogeweg, L., van Ginneken, B., Ayles, H., 2014. The sensitivity and specificity of using a computer aided diagnosis program for automatically scoring chest x-rays of presumptive TB patients compared with Xpert MTB/RIF in Lusaka Zambia. *PLoS One* 9, e93757. doi:10.1371/journal.pone.0093757.
- Muyoyeta, M., Moyo, M., Kasese, N., Ndhlovu, M., Milimo, D., Mwanza, W., Kapata, N., Schaap, A., Godfrey Faussett, P., Ayles, H., 2015. Implementation research to inform the use of Xpert MTB/RIF in primary health care facilities in high TB and HIV settings in resource constrained settings. *PLoS One* 10, e0126376. doi:10.1371/journal.pone.0126376.
- Porcel, J.M., 2009. Tuberculous pleural effusion. *Lung* 187, 263–270. doi:10.1007/s00408-009-9165-3.
- Porcel, J.M., Esquerda, A., Vives, M., Bielsa, S., 2014. Etiology of pleural effusions: analysis of more than 3,000 consecutive thoracenteses. *Arch. Bronconeumol.* 50, 161–165. doi:10.1016/j.arbres.2013.11.007.
- Roy, M., Ellis, S., 2010. Radiological diagnosis and follow-up of pulmonary tuberculosis. *Postgrad. Med. J.* 86, 663–674. doi:10.1136/pgmj.2009.084418.
- Samuelson, F., Petrick, N., 2006. Comparing image detection algorithms using resampling. In: *3rd IEEE International Symposium on Biomedical Imaging: Nano to Macro*, 2006, pp. 1312–1315. doi:10.1109/ISBI.2006.1625167.
- Shen, R., Cheng, I., Basu, A., 2010. A hybrid knowledge-guided detection technique for screening of infectious pulmonary tuberculosis from chest radiographs. *IEEE Trans. Biomed. Eng.* 57, 2646–2656. doi:10.1109/TBME.2010.2057509.
- Story, A., Aldridge, R.W., Abubakar, I., Stagg, H.R., Lipman, M., Watson, J.M., Hayward, A.C., 2012. Active case finding for pulmonary tuberculosis using mobile digital chest radiography: an observational study. *Int. J. Tuberc. Lung Dis.* 16, 1461–1467. doi:10.5588/ijtld.11.0773.
- Sutherland, J.S., Garba, D., Fombah, A.E., Mendy-Gomez, A., Mendy, F.S., Antonio, M., Townend, J., Ideh, R.C., Corrah, T., Ota, M.O.C., 2012. Highly accurate diagnosis of pleural tuberculosis by immunological analysis of the pleural effusion. *PLoS One* 7, e30324. doi:10.1371/journal.pone.0030324.
- Theron, G., Pooran, A., Peter, J., van Zyl-Smit, R., Mishra, H.K., Meldau, R., Calligaro, G., Allwood, B., Sharma, S.K., Dawson, R., Dheda, K., 2012. Do adjunct tuberculosis tests, when combined with Xpert MTB/RIF, improve accuracy and the cost of diagnosis in a resource-poor setting? *Eur. Respir. J.* 40, 161–168. doi:10.1183/09031936.00145511.
- Valdés, L., Alvarez, D., Valle, J.M., Pose, A., San José, E., 1996. The etiology of pleural effusions in an area with high incidence of tuberculosis. *Chest* 109, 158–162.
- World Health Organization, 2014. *Global tuberculosis report 2014*.
- Xu, T., Cheng, I., Long, R., Mandal, M., 2013. Novel coarse-to-fine dual scale technique for tuberculosis cavity detection in chest radiographs. *EURASIP J. Image Video Process.* 3, 1–18. doi:10.1186/1687-5281-2013-3.